Strength determination for rough substrate-coating interfaces with three-dimensional defect structure

T. Klünsner[a,*], M. Krobath[a], R. Konetschnik[b], C. Tritremmel[a], V. Maier-Kiener[b], D. Samardzic[a], W. Ecker[a], C. Czettl[c], C. Mitterer[b], D. Kiener[b]

[a] Materials Center Leoben Forschung GmbH, Roseggerstraße 12, 8700 Leoben, Austria
[b] Department of Materials Science, Montanuniversität Leoben, Franz-Josef-Straße 18, 8700 Leoben, Austria
[c] Ceratizit Austria GmbH, Metallwerk-Plansee Straße 71, 6600 Reutte, Austria

*Corresponding author:
Email address: thomas.kluensner@mcl.at

Abstract

Quantitative information on the strength of interfaces between thin ceramic coatings and their substrates is crucial when aiming to understand their failure behavior. Many technically relevant substrate-coating interfaces are not ideally planar, but rather rough and contain stress concentrators forming three-dimensional defect structures. An example for such a realistic case, a polycrystalline diamond coating that partially penetrates voids and cavities in its Co binder-depleted WC-Co hard metal substrate, was investigated within the current with respect to its interface strength. Special focus was laid on the influence of the applied load direction on the observed fracture behavior. Micromechanical specimens were produced via focused ion beam milling as geometry variants of a micro shear compression specimen with their loaded areas' relative inclination towards the substrate-coating interface of 0°, 30°, 45°, 60°, 75° and 88°. Specimen loading was performed until fracture with a flat punch indenter in a scanning electron microscope. The recorded fracture loads were associated with the spatial stress distributions at fracture via finite element-based analysis. A plateau of the determined maximum principal stress triggering fracture in the ceramic-ceramic interfaces was found for inclination angles ≥45°. This plateau value was identified as the interface strength by observation of the crack path at the substrate-coating interface via scanning electron microscopy and analysis of the effectively loaded interface area values.

Keywords

Interface strength; micromechanical test; defects; fracture; coated hard metal.

Graphical abstract

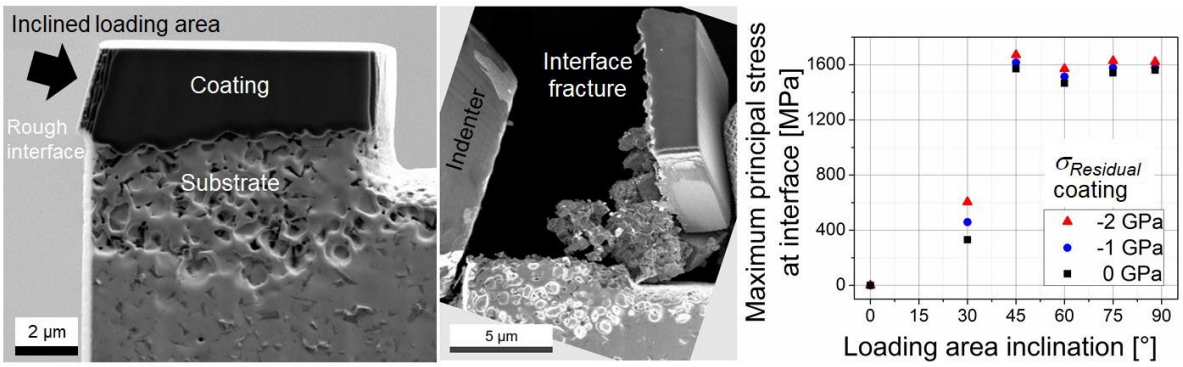

1. Introduction

In many applications the performance of components exposed to tribological loads is enhanced by thin ceramic coatings. For example, protective hard coatings are an established solution to enhance the productivity of metalworking tools in production processes such as milling, turning or drilling [1]. The loss of the coating in application is highly detrimental to the performance of the coated structure, e.g. a cutting edge of a milling tool that experiences accelerated wear when deprived of its coating [2]. Coating loss may be caused by wear or formation of cracks, e.g. those that propagate along the substrate-coating interface and lead to coating decohesion. Gradual coating wear is often the preferred failure mode of coated structures, since it does not occur suddenly as the formation of cracks. Coating decohesion is influenced by numerous factors such as the magnitude of load stresses compared to the substrate's yield strength [3], the load stress ratio [4] as well as residual stresses in coating [5],[6] and substrate [7], respectively. Tensile load components are most critical with respect to crack initiation and growth in homogeneous materials, as well as at interfaces between metallic phases [8] and even more so between ceramic materials [9]. This is especially relevant when interfaces themselves are not planar but three-dimensionally rough. A very general definition of three-dimensional (3D) interfaces was suggested in [10] as "*interfaces with hetero-phase character that extend out-of-plane into the two phases they join, and are chemically, crystallographically, and / or topologically divergent in three dimensions*". Interfaces with

a 3D defect structure are also given when interfacial inhomogeneities that act as sites of stress concentration reach out-of-interface-plane. A good example for such a case are diamond thin films on WC-Co hard metal substrates [11]. In this system, the metallic Co binder acts as a catalyst for the formation of graphite during chemical vapor deposition of the coating. Therefore, the Co is etched out of the substrate material to facilitate the growth of the coating in diamond structure and avoid the formation of graphite [12]. The etching gives rise to a binder-depleted zone in the WC-Co substrate with a rough surface and complex-shaped partially interconnected cavities that are in part filled by the coating during its deposition [13]. Coating decohesion is crucial to this system, since it hinders the further propagation of its use in machining of non-carbide forming metal components, where it has shown great potential to improve machining productivity [14].

A thorough understanding of the strength of interfaces between coatings and their substrates is essential when trying to understand and avoid coating decohesion. Most methods available for the characterization of the strength of interfaces only yield qualitative rankings for certain loading scenarios, but no quantitative interface strength information [15]. Typically, they also do not take account of the possible influence of a variation of the orientation of the external load on the determined strength value, i.e. a possible texture of a 3D interface defect structure. An example for the mentioned shortcomings are indentation techniques that lack the quantitative and inter-situative comparability of their results and currently do not allow for a direct control of the directions of the stresses that lead to interface failure [15],[16]. Also scratching-based methods lack quantitative result comparability due to the complex and transient stress fields arising at the tested interfaces [17],[18]. Micromechanical testing and interpretation of the stress-strain evolution during testing, combined with electron microscopy-based investigation of the µm-sized specimens can be used to address the discussed issues [19]. Some of the proposed methods enable to study interface strength by bending to impose a tensile load at interfaces [19],[20], use a push-to-shear device to impose shear stresses [21], or load interfaces that are inclined with respect to the direction of a compressive load [22],[23]. The last-mentioned techniques are interesting since in many applications, tension, compression and shear load components act simultaneously [24] and should thus be induced in laboratory test setups. Some documented efforts to do so have fallen short of demonstrating fracture at the studied strong interfaces [25], or induced strong plastification before plastic shear-off close to the studied metal/metal [22] and metal-ceramic interface [23] instead of interface fracture. Many proposed micromechanical test methods evaluate fracture properties of structures notched by focused ion beam (FIB) milling, also under multiaxial loading, but are not directly applicable for determination of substrate-coating interface strength [26],[27].

Another micromechanical test method uses a micro shear compression (MSC) specimen to induce fracture at ceramic-ceramic interfaces by the sought combination of tension, compression and shear load, with the quantitatively determined tensile load component, pointing in an out-of-interface-plane direction, referred to as the interface strength [28]. This geometry [28], however, is not yet capable of varying the applied load direction. Such possibility would be useful when studying the strength behavior of interfaces with a 3D

defect structure and the possible influence of defect-orientation effects, i.e. defect texture, on the observed strength.

The current work presents a material testing method involving modifications of an MSC specimen geometry. Its capability to induce interface fracture and to deliver quantitative interface strength values will be advanced to study the strength of larger interface areas with a 3D defect structure under variable external loading directions.

2. Methodological approach

2.1 Investigated materials

The samples investigated in the current work were made of a WC-Co hard metal (provided by Ceratizit Austria) with a Co binder content of 6 wt.% and an average WC grain size of 500 nm to 800 nm. The used samples had a cuboid shape with dimensions of 12.7 mm x 12.7 mm x 3.18 mm. The samples were job-coated with the commercially available nanocrystalline diamond coating of type BALINIT DIAMOND PLUS by Oerlikon Balzers in a chemical vapor deposition (CVD) process [12]. The average thickness of the diamond coating, determined via scanning electron microscopy (SEM) in a cross section prepared by FIB milling, was 8.5 µm, see Fig. 1a). The expected removal of all Co binder metal from the Co-depleted region of the substrate [12] was checked and confirmed by energy dispersive electron spectroscopy (EDX) mapping, see Fig. 1b).

2.2 Nanoindentation experiments

Nanoindentation experiments were conducted at room temperature on cross sections prepared via grinding and polishing using a nanoindenter (G200, Keysight, now KLA) equipped with a diamond Berkovich tip (Synton MDP, Nidau, Switzerland). 50 indentations were made in a rectangular pattern over the ion slicing polished sample cross section covering the three regions: CVD diamond, Co-depleted zone, and bulk WC-Co hard metal, see Fig. 1c). Only indents that were clearly assignable to a respective zone were evaluated - 16 indentations located at or close to a transition zone between the regions were therefore not taken into account. Hardness and Young's modulus were acquired at constant indentation strain rate (0.05 s^{-1}) to a preset indentation depth of 90 nm to 95 nm and were evaluated as proposed by Oliver & Pharr [29] from the continuous measurement of contact stiffness. Tip shape and frame stiffness calibrations with fused silica were performed at regular intervals. [30]

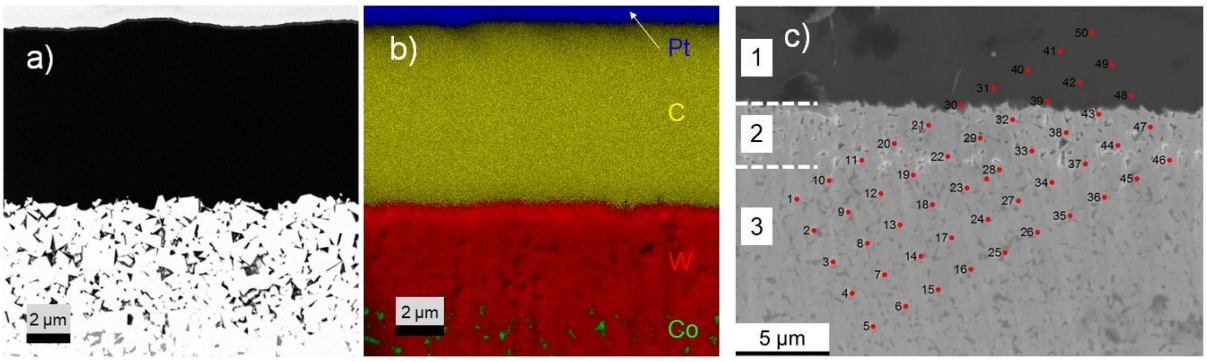

Fig. 1: SEM micrographs of cross sections of the investigated WC-Co hard metal sample coated with nanocrystalline diamond: a) FIB cut in backscattered electron contrast mode, b) image from a) with overlaid EDX scan to visualize the spatial distributions of the chemical elements Co (green), W (red), C (yellow), and Pt (blue – protective layer for FIB cutting), c) sites of the performed 50 nanoindentations indicated by red dots in the areas: 1: diamond coating, 2: Co binder-depleted zone, 3: bulk WC-Co hard metal [30]. For reference to color, the reader is referred to the online version of this article.

2.3 Micromechanical testing

To study the failure behavior of the substrate-coating interface, micromechanical tests were performed. The tested specimens were produced from the coated hard metal described in section 2.1 via cutting, grinding and polishing to yield a rectangular geometry with a minimal thickness of 300 µm. Subsequent thinning was performed using a low energy focused Ar^+ ion beam, which led to a minimum specimen thickness of 20 µm, thereby saving machining time during the final shaping step involving FIB milling [31]. The specimen geometries tested in the current work represent variants of an MSC specimen geometry introduced previously [28] to enable a variation of the direction of loading towards the substrate-coating interface. To this end, the orientations of the individual specimens loaded areas were varied stepwise from 0°, i.e. parallel orientation, towards the substrate-coating interface, via 30°, 45°, 60° and 75° to 88° relative inclination, see Fig. 2. The specimen variants shall hence be referred to as “micropillar” for the variant with parallel orientation of the loaded area towards the interface, and MSC-X°, with X referring to the respective relative inclination.

Specimen loading was performed using a conductive diamond flat punch indenter with 16 µm diameter (Synton-MDP, Nidau, Switzerland) mounted on an UNAT-1 (Asmec, Zwick-Roell, Germany) within a field emission SEM (LEO 982, Zeiss, Oberkochen, Germany) in directions indicated by thick white arrows in Fig. 2. The load was applied under displacement control with a constant displacement rate of 15 nm s^{-1}. A load-displacement curve was recorded for each compression fracture experiment. The specimen dimensions width *w*, depth *d* and maximum coating dimension in thickness direction *t*, as exemplarily indicated in Fig. 2a) and Fig. 2b), were determined after sample preparation via SEM. Due to FIB cutting characteristics, the specimen cross sections were slightly trapezoidal. The width values *w* given in Table I represent the mean values of specimen width determined at front and back side of the individual specimens. The Co-depleted zones had a thickness

of about 3.3 µm in all specimens. Note that the interface between coating and Co-depleted zone was rather rough and that it contained material inhomogeneities, hence referred to as defects, in the form of cavities and voids as marked by ovals in Fig. 2g). Also, the Co-depleted zone contained defects within its volume, as marked by thin arrows in Fig. 2g).

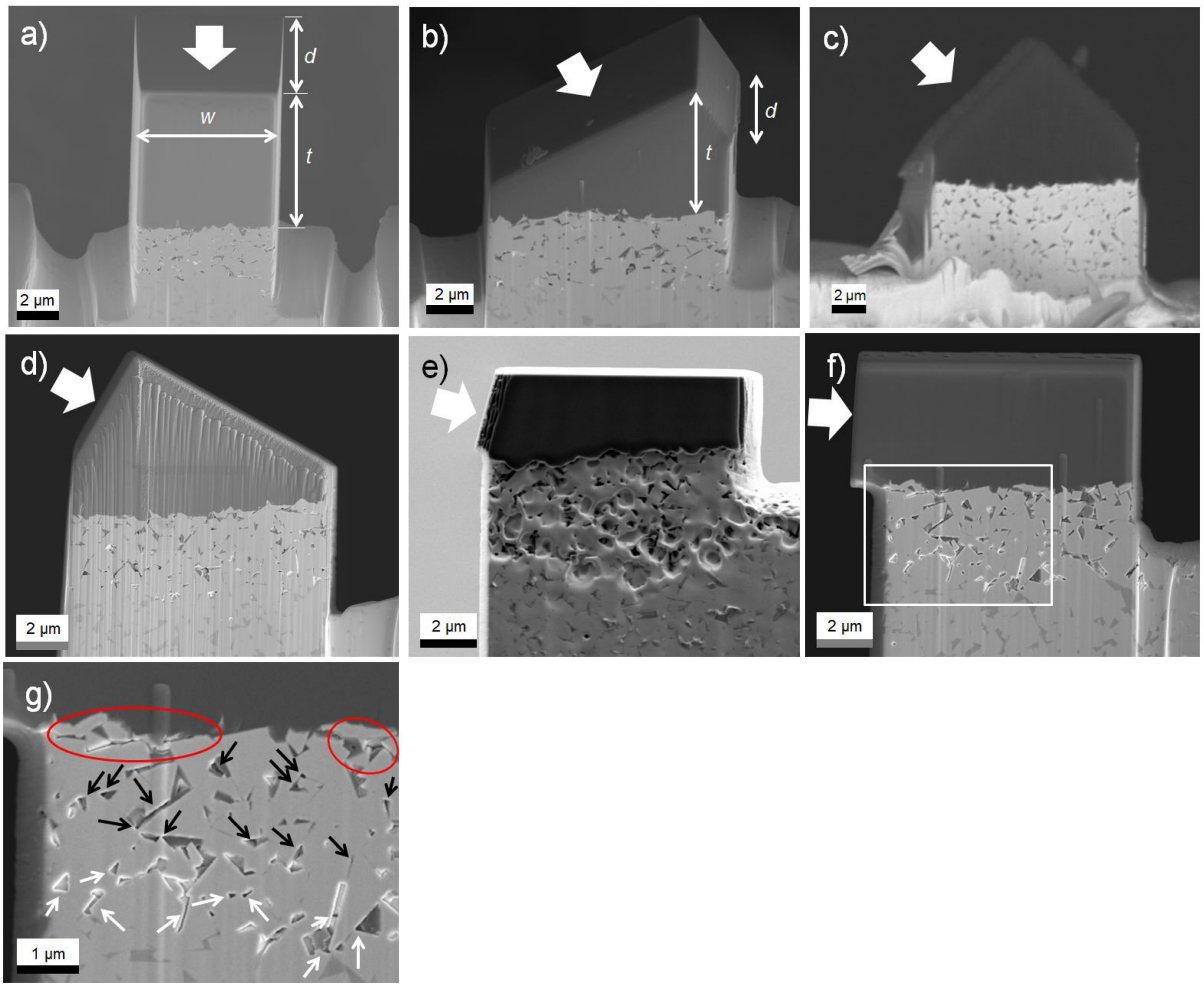

Fig. 2: SEM micrographs showing the investigated specimen geometries, whereby thick white arrows indicate the directions of loading. The areas of loading are inclined with respect to the substrate-coating interface by: a) 0° (micropillar), b) 30° (MSC-30°), c) 45°(MSC-45°), d) 60° (MSC-60°), e) 75° (MSC-75°), and f) 88° (MSC-88°). Note the inclined views in a) and b) to exemplarily show the dimensions width *w*, depth *d* and thickness *t*, respectively. The white frame in f) indicates a detail shown in g) with material inhomogeneities marked by ovals and thin arrows.

Table I: Dimensions of the investigated specimens determined by SEM, compare Fig. 2.

Specimen geometry	**Width *w* [µm]**	**Depth *d* [µm]**	**Thickness *t* [µm]**
Micropillar	7.1	7.8	8.4

MSC-30°	10.0	8.2	6.0
MSC-45°	11.6	10.8	8.2
MSC-60°	10.6	9.9	5.5
MSC-75°	9.8	10.0	2.5
MSC-88°	9.2	10.3	4.4

2.4 Finite element (FE) simulation

FE simulations were performed to study the spatial distribution of stress at the interfaces and within the Co-depleted zones of the investigated specimens at the respective experimentally determined fracture loads. The simulations were conducted using the commercial finite element software package Abaqus [32]. The specimen geometries used in the simulations displayed in Fig. 3 were constructed using the dimensions given in Table I. The slightly trapezoid shape of the horizontal specimen cross section was considered by using the mean value of the specimen width determined from front and back side measurements of the individual specimens, as given in Table I. The simulations did not consider any roughness of the loaded surfaces or interfaces, neither did they account for small possible misalignments between contacting surfaces of flat punch and loaded specimen, which can occur in real-world experiments [30]. Quantitative information on the 3D geometric shape distribution of the internal bulk notches in the Co-depleted zone of the specimen were not available or considered in the current FE model's assumptions. The geometry models of the investigated specimens are mounted on elastic WC-Co blocks, which represent the substrate regions of the individual experiments. The models with highly inclined loaded areas were placed at edges of the sample structure as in the experiments in which this was done to avoid collisions of indenter and sample.

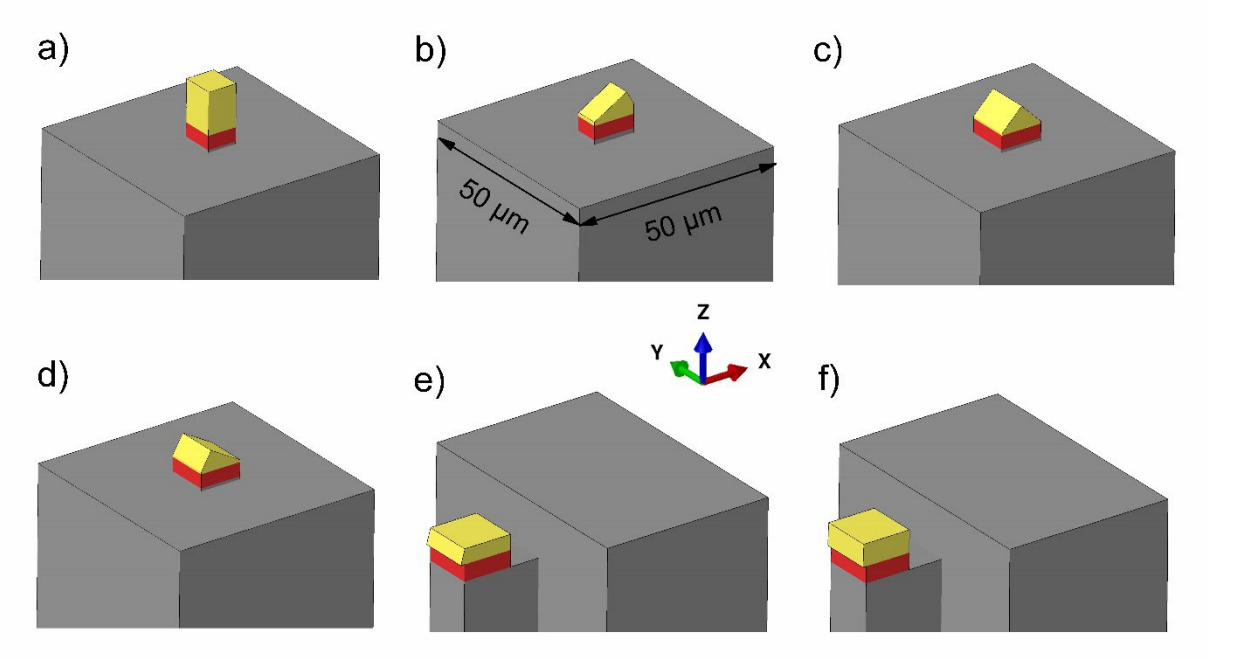

Fig. 3: Geometries of simulation models for the investigated specimens: a) micropillar, b) MSC-30°, c) MSC-45°, d) MSC-60°, e) MSC-75°, and f) MSC-88°. The different colors/shadings correspond to the material sections, i.e. from top to bottom: diamond (yellow), Co-depleted WC-Co (red), and WC-Co substrate (grey). For a), the indenter acts on the top face of the diamond region, whereas for all other cases, the indenter acts on the inclined left face of the diamond coating, compare Fig. 2.

Roughly 100.000 hexahedron elements with linear shape functions and reduced integration (C3D8R) were used to discretize the specimens. The element size close to the interfaces was approximately 0.1 µm. Linear elastic material behavior was assumed for all three relevant material sections with the relevant Young's moduli derived from nanoindentation experiments [30], see Table II. The listed Poisson ratios for CVD diamond and the hard metal were taken from [33] and [34], respectively. The Poisson ratio of the Co-depleted zone used in the simulation was slightly larger than for the solid composite WC-Co, according to FE-based predictions of the dependence of porous materials' lateral contraction behavior on porosity, pore shape and solid material Poisson ratio [35]. The volume removed by etching, resulting in the porosity of the Co-depleted zone, was assumed to be equivalent to the volume of Co binder metal, which is approximately 9 vol.%. The unknown exact residual stress value in the coating was considered in a physically reasonable range, with simulations performed without residual stress as well as with compressive residual stresses of -1000 MPa and -2000 MPa [36],[37], respectively. The Co-depleted zone and the WC-Co substrate were assumed as residual stress-free.

Table II: Hardness, Young's Modulus determined via indentation [30] and Poisson ratio of CVD diamond [33], Co-depleted zone [35] and hard metal [34].

Region of investigation	Hardness [GPa]	Young's Modulus [GPa]	Poisson ratio [-]
CVD diamond	71 ± 2.7	816 ± 24	0.069
Co-depleted hard metal	20 ± 2.4	472 ± 56	0.24
WC-Co hard metal	31 ± 4.8	689 ± 90	0.22

The effectively loaded volumes V_{eff} of the Co-depleted specimen regions were determined for the investigated specimens by evaluation of Eq. (1) [38]:

$$V_{eff} = \int \left(\frac{\sigma_1 H(\sigma_1)}{\sigma_{max}}\right)^{m_V} dV \quad (1)$$

There, V is the volume of the specimens' Co-depleted region, σ_1 the first principal stress, and σ_{max} is the maximum first principal stress in the Co-depleted specimen volume V. The Heaviside function $H(x)$ delivers 1 if $x \geq 0$ and zero if $x < 0$. It neglects compressive (negative) stress values and takes only tensile (positive) stresses into account. m_V is the Weibull modulus that describes the scatter of strength of the material volume which is currently unknown for the Co-depleted zone. Calculations of V_{eff} were performed for values of m_V including 20, 30 and 40, i.e. in a range of values known to occur in unetched WC-Co hard metals [39]. In the numerical implementation of Eq. (1), the integral was again substituted by a sum over all integration points. The stress was evaluated at the integration point level using the volume which is associated with each integration point.

To assess failure in the substrate-coating interface, an effectively loaded substrate-coating interface area A_{eff} was determined defined in analogy to V_{eff} for the investigated specimens:

$$A_{eff} = \int \left(\frac{\sigma_1 H(\sigma_1)}{\sigma_{max}}\right)^{m_I} dA \quad (2)$$

There, A refers to the area of the substrate-coating interface – in particular the interface between the Co-depleted zone and the diamond coating, σ_1 is the first principal stress, and σ_{max} is the maximum first principal stress in the interface. m_I is the Weibull modulus that describes the scatter of interface strength. Its value is currently unknown for the investigated interface due to an insufficient number of strength experiments [9]. Calculations of A_{eff} were performed for 16 values of m between 5 and 80 with a step size of 5. In the numerical implementation of Eq. (2), the integral was again substituted by a

sum over all involved integration points. The stress was evaluated at the individual integration points using the integration point's associated interface area.

3. Results and discussion

The load-displacement data recorded during specimen loading from initial indenter-specimen contact until the moment of specimen fracture are displayed in Fig. 4. All tested samples exhibit brittle behavior, with linear elastic loading followed by rapid catastrophic failure. Note that the observed different slopes for the individual experiments result from different compliances of the respective indenter-specimen geometry combinations. However, for the further quantitative considerations regarding the fracture behavior, the load at fracture is of most relevance.

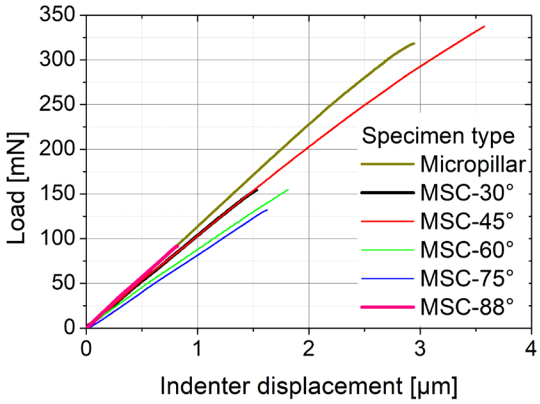

Fig. 4: Load-displacement data until fracture under compression for the investigated specimens: micropillar, MSC-30°, MSC-45°, MSC-60°, MSC-75°, and MSC-88°; compare Fig. 2 for the respective labels. For reference to color, the reader is referred to the online version of this article.

The respective SEM micrographs of the specimens' state after fracture are provided in Fig. 5. For an animated impression of the conducted experiments, see the videos in the supplementary material. In Fig. 5a), fragments of the specimen with intact interface between diamond coating and substrate are still visible, with two crack planes running roughly perpendicular to the loaded coating surface of the micropillar. This observation indicates that the propagation of fracture did not occur at the substrate-coating interface in this specimen. As seen in Fig. 5b) and Fig. 5c), the specimens MSC-30° and MSC-45° were destroyed by the elastic spring back of the indenter, i.e. a sudden distinct displacement increase, due to the release of elastic energy stored in the loaded assembly of indenter and specimen. Therefore, it was impossible to attain information regarding the origin or propagation path of the crack that lead to failure of these two specimens. In contrast, evidence for crack propagation at the substrate-coating interface can be gained from the attained SEM micrographs for three of the investigated specimens, namely for

MSC-60°, MSC-75° and MSC-88°, see Fig. 5d), Fig. 5e) and Fig. 5f), respectively. A comparison of the contours of the interface before fracture and the detached coating fragment's lower side after fracture, compare Fig. 2e) and Fig. 5e), provides a clear indication that crack nucleation and propagation occurred along the interface in the case of MSC-75°.

The elastic indenter spring back partly damaged the remains of specimens MSC-60° and MSC-88° after specimen fracture by crushing their sides facing the indenter, see Fig. 5d) and Fig. 5f), respectively. Still, undamaged crack flank portions of equal shape remain at the bottom side of the coating and top side of the substrate, see white and black ovals in Fig. 5d) and Fig. 5f), indicating that crack nucleation and propagation occurred at the substrate-coating interface. The crack path deviations away from the interface after having crossed some of the specimens' cross-section, as observed in Fig. 5d) and Fig. 5f), can be rationalized by considering that in brittle solids cracks can reach velocities in the order of considerable fractions of the speed of sound [40]. The indenter approaching the specimens from the left-hand side imposed some bending loading with compressive loads portions at the right-hand specimen side. Because the cracks propagate about as fast as internal stresses can relax in the later stages of their accelerated propagation, they avoid regions still under compressive stress as they approach, by changing direction and deviating from their initial path along the interface. This phenomenon is also known as "compression curl" [41].

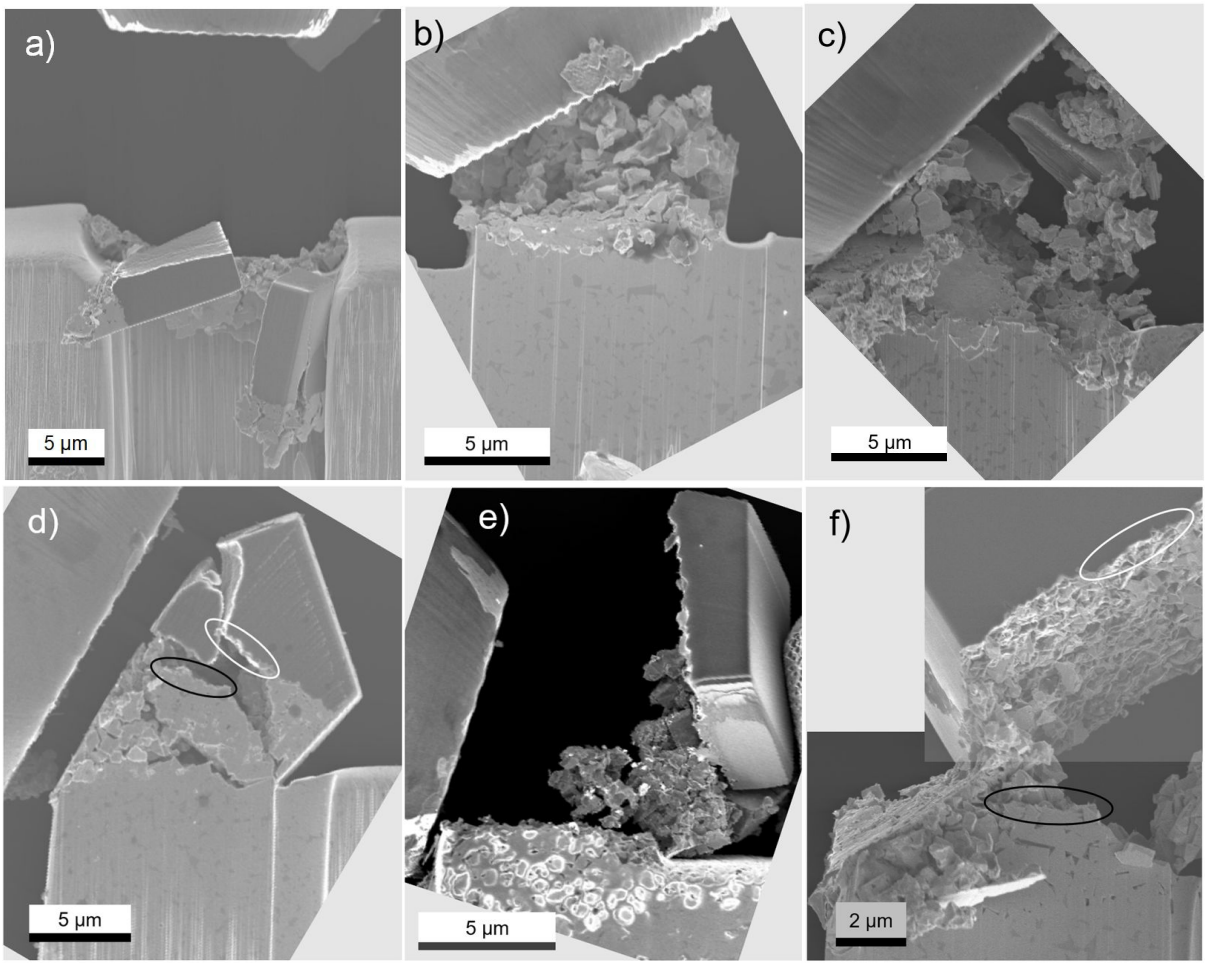

Fig. 5: SEM micrographs of the specimens after fracture: a) micropillar, b) MSC-30°, c) MSC-45°, d) MSC-60°, e) MSC-75°, and f) MSC-88°. Corresponding sites on the fracture surfaces on substrate and coating side are marked by black and white ovals in d) and f), respectively.

The given differences in specimen geometry, size, interfacial area and loading direction with respect to the substrate-coating interface demanded a detailed assessment of the stresses acting in the specimens at the moment of fracture. The FEM-based evaluation of spatial stress distributions was focused on the Co-depleted zone including the interface towards the coating for all geometries, as SEM micrographs indicated interface fracture for three out of six investigated specimen types, compare Fig. 5. The 3D contour plots of the spatial distributions of the maximum principal stress at and below the substrate-coating interface at fracture load are shown in Fig. 6. The top face in each subfigure represents the interfaces between diamond coating and Co-depleted WC-Co. The exemplarily shown cases represent the calculations for the most reasonable value of 1 GPa compressive residual stress in the coating [36],[37]. When comparing the distributions in Fig. 6, it is apparent that the concentration of maximum principle stress becomes more pronounced with rising relative inclination between loaded area and interface. Assuming equal probability of failure of bulk and interface regions, this is a factor fostering interface fracture.

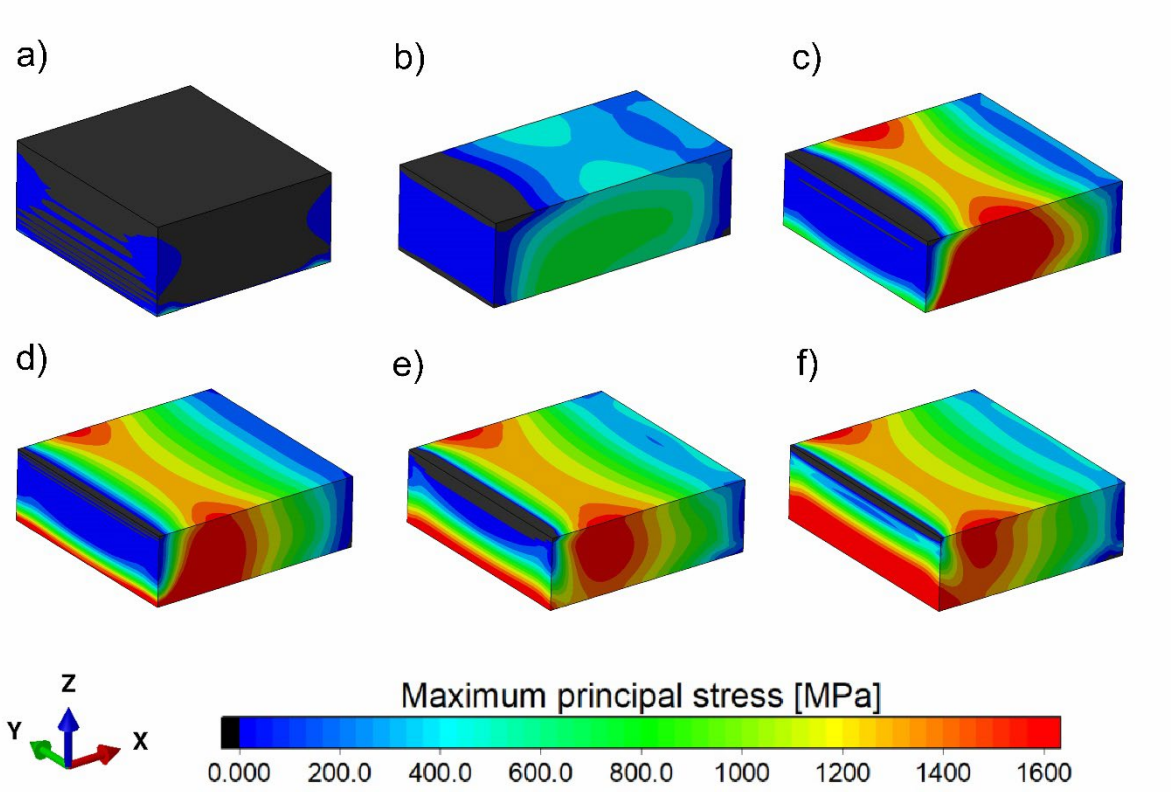

Fig. 6: Maximum principal stress distribution in the Co-depleted zones at fracture load for the specimens: a) micropillar, b) MSC-30°, c) MSC-45°, d) MSC-60°, e) MSC-75°, and f) MSC-88° for 1 GPa compressive residual stress in the diamond coating. The top face represents the interface between diamond and Co-depleted WC-Co. For reference to color, the reader is referred to the online version of this article.

Fig. 7a) displays the largest values of maximum principal stress acting at the substrate-coating interface of all investigated specimens. The maximum principal stress at the interface of the micropillar has a value of zero for all assumed residual stress states, see Fig. 7a). This corroborates the conclusions drawn from the available fractographic evidence from Fig. 5a), namely that fracture did not start at the interface in this specimen type. The maximum principle stress value determined for MSC-30° is greater than zero and rises with increasing assumed compressive residual stress in the coating. This makes sense, as in-plane compression gives rise to out-of-plane tension due to a buckling tendency of the coating [42]. The determined orientations of the maximum principal stresses indicated by the green double arrows in Fig. 7a) are about perpendicular to the direction of the external loads. This can be rationalized considering that the tensile stresses are induced by lateral strains oriented about perpendicular to the external load. The mentioned stress values determined for MSC-30° cannot be interpreted physically in a concise fashion, since the specimen was destroyed by the indenter spring back and no information about the fracture path is available. Strikingly, the maximum principal stresses at fracture determined for the MSC specimens with inclination angles ≥45° assume a plateau value of about 1600 MPa. The evidence for crack origination and propagation at the interfaces of MSC-60°, MSC-75° and MSC-88°, see Fig. 5d) to Fig. 5f), suggests that

this stress plateau can be related to an interface strength property. The determined strength values are influenced by the unknown exact value of residual stress in the coating, as described before for the case of MSC-30°.

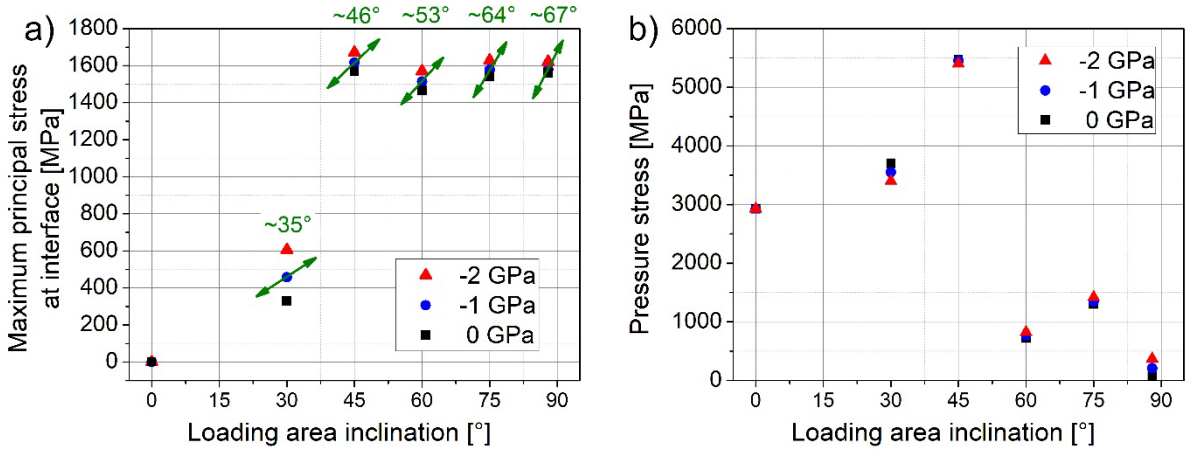

Fig. 7: Local maxima of stress at fracture load for the MSC-X° specimens with different loading area inclinations X with respect to their internal substrate-coating interface: a) maximum principal stress at the interface between diamond coating and Co-depleted WC-Co. Double arrows represent the stress direction with respect to the horizontal interface; b) pressure stress in the volume of the Co-depleted zone. Three residual stress states of the diamond coating were evaluated for each specimen: -2, -1 and 0 GPa, respectively.

The largest absolute values of the pressure stress, i.e. the negative one-third of the trace of the stress tensor, acting in the volumes of the Co-depleted zones at the moment of fracture, are displayed in Fig. 7b). Compared to the specimens MSC-60° to MSC-88°, the level of pressure stress acting in the volumes of the micropillar, MSC-30° and MSC-45° at the moment of fracture is significantly higher, see Fig. 7b). A possible interpretation of this observation is that a change in fracture mode from interface fracture to fracture originating in the substrate bulk is fostered by high pressure stress values. Tensile stresses that may trigger failure of specimens with high levels of pressure stress can be caused by compression at notches – also equiaxed ones – in the bulk of the Co-depleted zone. Note that the highest pressure stress value was found for the MSC-45° specimen in the current comparison, see Fig. 7b). Since the largest maximum principle stress determined at fracture load of this specimen is far lower than the pressure stress value, and quasi equal to the so-interpreted interface strength plateau value, it is likely that failure was triggered at the interface of this specimen.

Note that the well-known size effect on strength predicts an inverse relation of effectively loaded area or volume with the fracture stress observed in strength experiments for brittle materials [9]. The same concept is applied here to the interface area A_{eff}. Fig. 8a) shows the A_{eff} results for all investigated specimens for the unknown Weibull moduli m_I in the range of $10 \leq m_I \leq 50$. The m_I values 20, 30 and 40 are considered as a likely relevant value range, as it is observed in unetched WC-Co hard metals [39]. The A_{eff} results for this range are shown in Fig. 8b) as a function of the loaded area's inclination. From Fig.

8a) and Fig. 8b) it becomes apparent that the smallest value of interface strength determined for MSC-60°, see Fig. 7a), coincides with the maximum of the effectively loaded interface area of all investigated specimens. There is no apparent correlation of the individual values of the stress plateau with the values of the effectively loaded volume V_{eff} of the Co-depleted zone of the specimens, that is shown in Fig. 8c) as a function of the loaded area's inclination. In combination, these findings corroborate the notion that fracture actually originated at the interface and not in the volume of the Co-depleted zone of the specimens that formed the maximum principal stress plateau in Fig. 7a). This also means that the maximum principle stress plateau in Fig. 7a) actually represents the interface strength.

The origins of the cracks that lead to failure in those specimens that form the strength plateau in Fig. 7a) are interpreted to be of similar nature as the defects located at or just below to the substrate-coating interface indicated exemplarily by the red ovals in Fig. 2f). These defects form sites of stress concentration with a volatile spatial orientation. This gives rise to rough fracture surfaces, as visible in Fig. 5d) to Fig. 5f). The 3D shape of these fracture surfaces is visible most clearly in the case of MSC-88° below the white oval in Fig. 5f). The wide range of orientations of the facets on this fracture surface, along which the crack propagated, gives an impression of the 3D arrangement of the defects present at the tested interfaces. Evidently, the partial penetration of the diamond coating into the Co-depleted zone left behind cavities that remained effective stress concentrators located either directly at the substrate-coating interface, or just below the topmost WC grain adjacent to the coating. After nucleation, the cracks preferred to propagate along a path featuring these mentioned locations, at least before deviating from it in the last section of their path due to stress relaxation kinetics as described before. Thus, the investigated interface fulfills the definition of a 3D interface [10] and its dimensionality D is not described by $2 < D < 3$, as in descriptions of surfaces or interfaces as fractal-like objects [43] with a similarity cut-off at the nm length scale [44].

The apparent insensitivity of the determined strength values to the orientation change of the maximum principal stress with respect to the substrate-coating interface, indicated by the green double-arrows in Fig. 7a), can be rationalized as follows: The defects at or just below the interface approximate prismatic-shaped cavities that exhibit variable orientations, compare left and right oval in Fig. 2f). During loading, the largest and sharpest interfacial notch, with its longest axis orientated most perpendicular towards the external load, experienced the largest stress concentration and formed the origin of fracture. Note that the largest individual WC grains were identified to be origins of bulk fracture for small values of V_{eff} for the investigated type of substrate material in the unetched state for a wide range of possible microstructures [45]. In general, the etching procedure performed prior to coating deposition leads to removal of the Co binder phase and leaves behind a contiguous skeleton of WC grains with cavities [12]. It can therefore be assumed that the size of defects at the investigated interface is proportional to the size of the WC grains. It seems thus reasonable that the about 230 WC grains present at the substrate-sides of the approximately 100 µm²-sized investigated interfaces, cf. Table I, are sufficient to yield representative information on the interface defect population, i.e. the

interface strength. They apparently were sufficient to indicate representative information on the interface strength, even though the exact sizes of A_{eff} were not determined quantitatively, compare Fig. 8, due to the unknown Weibull modulus m_I.

Interface strength scaling with A_{eff} is very likely to be generally relevant, as in the known case of V_{eff} variation, for which the observed strength behavior changes significantly when V_{eff} values, e.g. of metalworking tools [46], surpass a certain limit in application. Then, a second, on average larger, defect type of a globally bi-modal defect size distributions was observed to become fracture-relevant [39]. In this respect, one should consider that interface inhomogeneities can be present only at specific lateral locations of the substrate-coating interface, e.g. as documented for a location close to the cutting edge of a hard-coated metalworking tool [47]. In such a case, interface strength tests should be performed on the specific locations at which inhomogeneities are to be expected and on such ones without their presence to assess their relevance. In this context, the distinction between Weibull moduli m_I and m_V, describing the respective strength scatter of interface and material bulk made in the current work is relevant in quantitative failure probability assessment of coated structures.

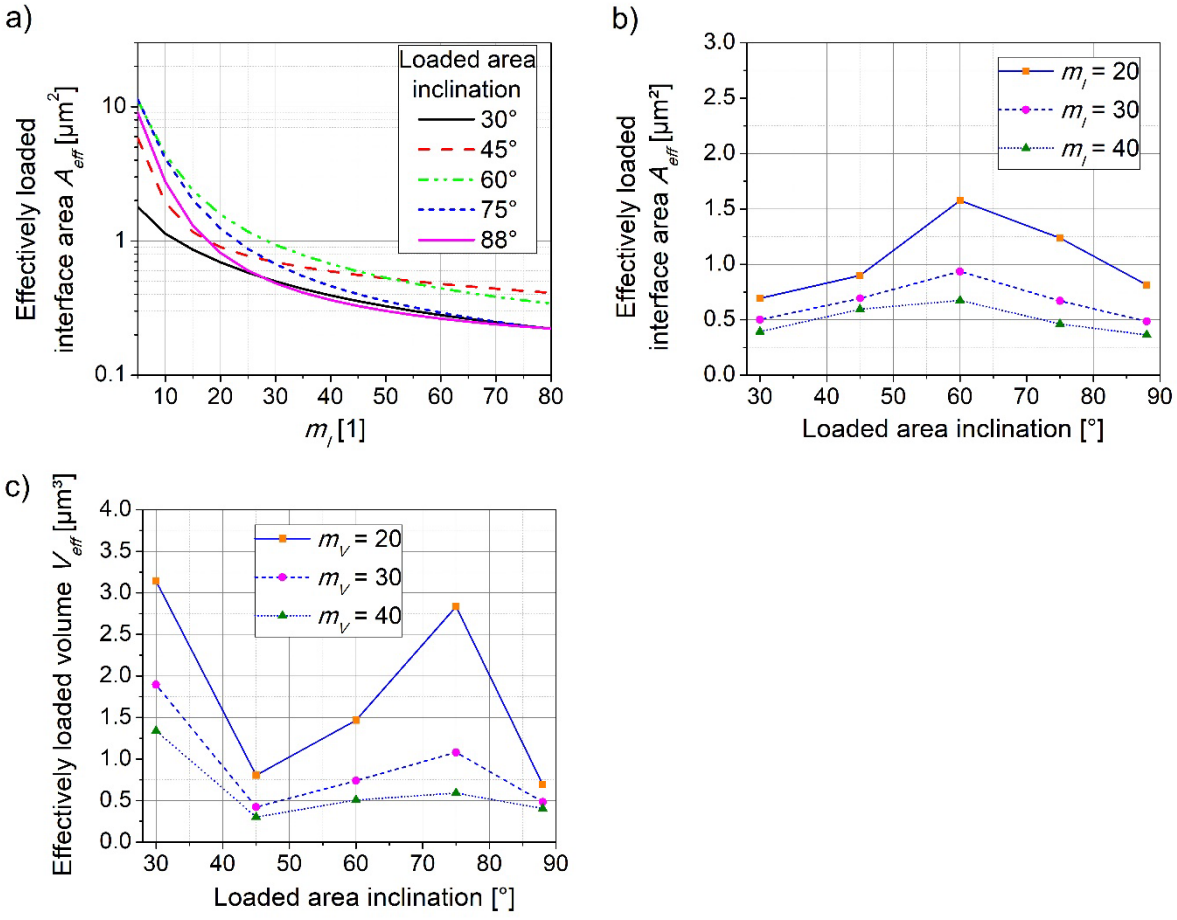

Fig. 8: Effectively loaded interface area A_{eff} of the interface between diamond coating and Co-depleted WC-Co over: a) Weibull modulus m_I for the investigated loaded area inclinations, b) loading angles for three values of m_I. c) Effectively loaded volume V_{eff} of the Co-depleted WC-Co zone for the investigated loaded areas inclinations for three Weibull moduli m_V.

It can be recommended to use MSC specimens with relative inclinations between loaded area and investigated interface ≥60°, especially when trying to determine interface strength in single MSC specimen geometry type experiments as executed in [28]. Below that angle, bulk fracture initiation is fostered by: i) pressure stress components contributing significantly to the stress state, and ii) the shift of the peak of the maximum principle stress distribution towards the bulk with lower relative inclination between loaded area and interface, as mentioned when discussing Fig. 6.

Future applications of the currently proposed technique could be aimed at determination of interface strength changes that result when substrate-coating systems with three-dimensionally rough interfaces are intentionally modified to enhance their properties. An example for such an effort is diamond-coated hard metal with its substrate's Co-depleted zone's cavities filled with a metallic diffusion layer, e.g. Ta, to enhance coating-substrate adhesion as described in [48]. Changes in the fracture mode depending on the load orientation and a possible introduction of an interface defect texture may be associated with this kind of interface modification. Also, cavities with some distance from the substrate-coating interface in the Co-depleted zone, see arrows in Fig. 2f), could unintentionally remain unfilled with the diffusing Ta metal, becoming the locations of highest stress concentration and thus trigger bulk fracture. A thorough investigation of the influence of the involved values of the used specimen's V_{eff} and A_{eff} in application-relevant size regimes on the observed strength behavior is recommendable. Last, but not least, the performance of the described experiments at elevated temperatures, as relevant for many applications [49], could yield quantitative information on the influence of temperature on interface fracture strength.

4. Conclusions

The current work investigated the strength properties of the interface between a nanocrystalline CVD diamond coating and the near-surface zone in a WC-Co hard metal substrate that was depleted of its metallic Co binder by etching. The formed interface featured a three-dimensional defect structure influenced by partial penetration of the coating into cavities present in the substrate. Micromechanical testing was performed using a micropillar and five geometry variants of the micro shear compression specimen geometry with a systematic variation of the inclination between the applied load and the above-mentioned interface from 0° to 88°. Finite element-based analysis revealed quasi-constant values of the maximum principal stress at fracture for the loaded area's inclination towards the substrate-coating interface of 45°, 60°, 75° and 88°. Since for three of the four investigated cases cracks were observed to propagate at the interface, the constant value of fracture stress was interpreted as the strength of this complex 3D interface.

The ceramic nature of the materials that form the investigated interface suggests that their fracture behavior is governed by the size and orientation of the defects present in a 3D arrangement of cavities partially penetrated by the coating. The determined constant interface strength value indicates that: a) neither the low-symmetry geometry of the

cavities, nor the partial penetration of the diamond coating into the Co-depleted zone lead to a strong dependence of the interface strength on the direction of load application (defect texture), and b) the determined strength value is representative for the interface strength for the imposed effectively tested interface area of about 100 μm². The proposed materials testing technique facilitates future efforts to improve the quantitative understanding of the strength behavior of interfaces with three-dimensional defect structure. Especially the dependence of interface strength on defect size distribution, defect texture and the interface area size effect on strength remains still widely unexplored.

Dedication

In the early stages of the current work, our dear colleague Dr. Roland Barbist unexpectedly passed away. The authors want to acknowledge the inspiration he provided to his younger colleagues with his passion for research. We want to express our compassion with his family that will miss him the most.

Supplementary material

Note that in the shown videos, the indenter approaches the specimens from the right hand side, while the images in Fig. 5 were mirrored and/or rotated to ease understanding of the systematic variation of the loading situations.

Acknowledgements

The authors gratefully acknowledge the financial support under the scope of the COMET program within the K2 Center “Integrated Computational Material, Process and Product Engineering (IC-MPPE)” (Project No 886385). This program is supported by the Austrian Federal Ministries for Climate Action, Environment, Energy, Mobility, Innovation and Technology (BMK) and for Digital and Economic Affairs (BMDW), represented by the Austrian Research Promotion Agency (FFG), and the federal states of Styria, Upper Austria and Tyrol. Daniel Kiener acknowledges funding from the European Research Council (ERC) under the European Union’s Horizon 2020 research and innovation programme (Grant No. 771146 TOUGHIT). Additional tasks related to the current work performed by Philipp Thomma and Johannes Glätzle are also gratefully acknowledged.

References

[1] F. Klocke, Manufacturing Processes 1 - Cutting, RWTH, Springer-Verlag Berlin Heidelberg, Aachen, 2011. https://doi.org/10.1007/978-3-642-11979-8.
[2] S. Gao, M. Zheng, J. Zhu, J. Chen, Mechanism of adhesion failure during interrupted cutting with cemented carbide tools: Experimental and ab-initio perspective, Int. J. Refract. Met. Hard Mater. 98 (2021) 105549. https://doi.org/10.1016/j.ijrmhm.2021.105549.
[3] T. Klünsner, M. Krobath, W. Ecker, S. Marsoner, M. Morstein, B. Marklein, Influence of localized cyclic substrate plastification on residual stress, load stress and cracking near the interface between hard coating and WC-Co hard metal substrate, Int. J. Refract. Met. Hard Mater. 82 (2019) 113–120. https://doi.org/10.1016/j.ijrmhm.2019.04.003.
[4] T. Klünsner, S. Marsoner, R. Ebner, R. Pippan, J. Glätzle, A. Püschel, Effect of microstructure on fatigue properties of WC-Co hard metals, Proc. Eng. 2 (2010) 2001–2010. https://doi.org/10.1016/j.proeng.2010.03.215.
[5] M. Tkadletz, J. Keckes, N. Schalk, I. Krajinovic, M. Burghammer, C. Czettl, C. Mitterer, Residual stress gradients in α-Al2O3 hard coatings determined by pencil-beam X-ray nanodiffraction, Surf. Coat. Technol. 262 (2015) 134–140. https://doi.org/10.1016/j.surfcoat.2014.12.028.
[6] L. Faksa, W. Daves, T. Klünsner, K. Maier, T. Antretter, C. Czettl, W. Ecker, Shot peening-induced plastic deformation of individual phases within a coated WC-Co hard metal composite material including stress-strain curves for WC as a function of temperature, Surf. Coat. Technol. 380 (2019) 125026. https://doi.org/10.1016/j.surfcoat.2019.125026.
[7] T. Klünsner, M. Morstein, S. Marsoner, M. Deller, B. Marklein, Fatigue life equality of polished and electrical discharge machined WC-Co hard metal achieved solely by wet blasting, Int. J. Refract. Met. Hard Mater. 59 (2016) 61–66. http://dx.doi.org/10.1016/j.ijrmhm.2016.05.001.
[8] C.H. Hsieh, C.H. Chang, W.S. Chuang, X. Wang, J.C. Huang, Tension behavior of interfaces between ZrCu metallic glass and Si or Zr, Appl. Surf. Sci. 356 (2015) 416-421. http://dx.doi.org/10.1016/j.apsusc.2015.08.092.
[9] R. Danzer, T. Lube, P. Supancic, R. Damani, Fracture of ceramics, Adv. Eng. Mater. 10 (2008) 275–298, https://doi.org/10.1002/adem.200700347.
[10] Y. Chen, N. Li, R.G. Hoagland, X.-Y. Liu, J.K. Baldwin, I.J. Beyerlein, J.Y. Cheng, N.A. Mara, Effects of three-dimensional Cu/Nb interfaces on strengthening and shear banding in nanoscale metallic multilayers, Acta Mater. 199 (2020) 593–601. https://doi.org/10.1016/j.actamat.2020.08.019.
[11] V.K. Sarin, D. Mari, L. Llanes, C.E. Nebel, Comprehensive Hard Materials - Hardmetals, 1, Elsevier, Oxford, 2014. http://dx.doi.org/10.1016/B978-0-08-096527-7.00001-5.
[12] R. Haubner, W. Kalss, Diamond deposition on hardmetal substrates - Comparison of substrate pre-treatments and industrial applications, Int. J. Refract. Met. Hard Mater. 28 (2010) 475–483. https://doi.org/10.1016/j.ijrmhm.2010.03.004.
[13] S.A. Linnik, A.V. Gaidaichuk, V.V. Okhotnikov, Influence of Cobalt on the Adhesion Strength of Polycrystalline Diamond Coatings on WC–Co Hard Alloys, Tech. Phys+. 63 (2018) 206–210. https://doi.org/10.1134/S1063784218020226.
[14] Z. Zhang, W. Lu, W. Feng, X. Du, D. Zuo, Effect of substrate surface texture on adhesion performance of diamond coating, Int. J. Refract. Met. Hard Mater. 95 (2021) 105402. https://doi.org/10.1016/j.ijrmhm.2020.105402.
[15] Z. Chen, K. Zhou, X. Lu, Y.C. Lam, A review on the mechanical methods for evaluating coating adhesion, Acta Mech. 225 (2014) 431–452. https://doi.org/10.1007/s00707-013-0979-y.
[16] N. Vidakis, A. Antoniadis, N. Bilalis, The VDI 3198 indentation test evaluation of a reliable qualitative control for layered compounds, J. Mater. Process. Technol. 143–144 (2003) 481–485. https://doi.org/10.1016/S0924-0136(03)00300-5.

[17] X. Wang, P. Xu, R. Han, J. Ren, L. Li, N. Han, F. Xing, J. Zhu, A review on the mechanical properties for thin film and block structure characterised by using nanoscratch test, Nanotechnol. Rev. 8 (2019) 628-644. https://doi.org/10.1515/ntrev-2019-0055.
[18] S.J. Bull, E.G. Berasetegui, An overview of the potential of quantitative coating adhesion measurement by scratch testing, Tribol. Int. 39 (2006) 99-114. https://doi.org/10.1016/j.triboint.2005.04.013.
[19] K. Matoy, T. Detzel, M. Müller, C. Motz, G. Dehm, Interface fracture properties of thin films studied by using the micro-cantilever deflection technique, Surf. Coatings Technol. 204 (2009) 878–881. https://doi.org/10.1016/j.surfcoat.2009.09.013.
[20] R. Konetschnik, R. Daniel, R. Brunner, D. Kiener, Selective interface toughness measurements of layered thin films, AIP Adv. 7 (2017). https://doi.org/10.1063/1.4978337.
[21] M. Alfreider, G. Balbus, F. Wang, J. Zechner, D.S. Gianola, D. Kiener, Interface mediated deformation and fracture of an elastic–plastic bimaterial system resolved by in situ transmission scanning electron microscopy, Mater. Des. 223 (2022) 111136. https://doi.org/10.1016/j.matdes.2022.111136
[22] M.C. Liu, J.C. Huang, Y.T. Fong, S.P. Ju, X.H. Du, H.J. Pei, T.G. Nieh, Assessing the interfacial strength of an amorphous-crystalline interface, Acta Mater. 61 (2013) 3304–3313. https://doi.org/10.1016/j.actamat.2013.02.019.
[23] X. Zhang, B. Zhang, Y. Mu, S. Shao, C.D. Wick, B.R. Ramachandran, W.J. Meng, Mechanical failure of metal/ceramic interfacial regions under shear loading, Acta Mater. 138 (2017) 224.236. https://doi.org/10.1016/j.actamat.2017.07.053.
[24] T. Kaltenbrunner, K. Maier, T. Klünsner, H.P. Krückl, M. Krobath, M. Pötz, J. Wosik, O. Binder, T. Teppernegg, C. Czettl, W. Ecker, Combined experimental and numerical analysis of critical loading conditions for hard metal tool damage in titanium milling, J. Manuf. Process. 77 (2022) 125–137. https://doi.org/10.1016/j.jmapro.2022.02.059.
[25] I. El Azhari, J. García, M. Zamanzade, F. Soldera, C. Pauly, C. Motz, L. Llanes, F. Mücklich, Micromechanical investigations of CVD coated WC-Co cemented carbide by micropillar compression, Mater. Des. 186 (2020). https://doi.org/10.1016/j.matdes.2019.108283.
[26] J. Ast, J.J. Schwiedrzika, N. Rohbeck, X. Maeder, J. Michler, Novel micro-scale specimens for mode-dependent fracture testing of brittle materials: A case study on GaAs single crystals, Mater. Des. 193 (2020) 108765. https://doi.org/10.1016/j.matdes.2020.108765.
[27] N.G. Mathews, A.K. Mishra, B.N. Jaya, Mode dependent evaluation of fracture behaviour using cantilever bending, Theoret. Appl. Fract. Mechanics 115 (2021) 103069. https://doi.org/10.1016/j.tafmec.2021.103069.
[28] M. Gsellmann, T. Klünsner, C. Mitterer, M. Krobath, M. Wurmshuber, H. Leitner, W. Ecker, S. Marsoner, V. Maier-Kiener, D. Kiener, G. Ressel, Strength ranking for interfaces between a TiN hard coating and microstructural constituents of high speed steel determined by micromechanical testing, Mat. Des. 204 (2021) 109690. https://doi.org/10.1016/j.matdes.2021.109690.
[29] W.C. Oliver, G.M. Pharr, An improved technique for determining hardness and elastic modulus using load and displacement sensing indentation experiments, J. Mater. Res. 7 (1992) 1564-1583. https://doi.org/10.1557/JMR.1992.1564.
[30] P. Thomma, C. Tritremmel, T. Klünsner, C. Czettl, C. Mitterer, Micromechanical testing of CVD diamond coated WC-Co hard metal, Proc. 19th Plansee Seminar, 2017, Reutte in Tirol, Austria.
[31] S. Wurster, R. Treml, R. Fritz, M.W. Kapp, E. Langs, M. Alfreider, C. Ruhs, P.J. Imrich, G. Felber, D. Kiener, Novel Methods for the Site Specific Preparation of Micromechanical Structures, Pract. Metallogr. 52 (2015) 131–146.

[32] Abaqus 2018, Dassault Syst. Simulia Corp. 2018. https://www.3ds.com/ (last accessed 27/07/2022)
[33] http://usapplieddiamond.com/wp-content/uploads/2016/02/chart3.pdf (last accessed 29/07/2022)
[34] T. Teppernegg, T. Klünsner, C. Kremsner, C. Tritremmel, C. Czettl, S. Puchegger, S. Marsoner, R. Pippan, R. Ebner, High temperature mechanical properties of WC-Co hard metals, Int. J. Refract. Met. Hard Mater. 56 (2016) 139.144. https://doi.org/10.1016/j.ijrmhm.2016.01.002.
[35] T. Uhlířová, W. Pabst, Poisson's ratio of porous and cellular materials with randomly distributed isometric pores or cells, J. Am. Ceram. Soc. 103 (2020) 6961-6977. https://doi.org/10.1111/JACE.17139.
[36] E. Uhlmann, F. Sammler, M. Meixner, D. Heinrich, F. Gansert, W. Reimers, D. Berger, I. Rieck, Analysis of residual stresses and wear mechanism of HF-CVD diamond coated cemented carbide tools, Prod. Eng. Res. Devel. 9 (2015) 99-107. DOI 10.1007/s11740-014-0580-9.
[37] D. Hinzmann, K. Böttcher, W. Reimers, E. Uhlmann, Ex Situ Residual Stress Analysis of Chemical Vapor Deposited Diamond Coated Cutting Tools by Synchrotron X-Ray Diffraction in Transmission Geometry, Adv. Eng. Mater. 23 (2021) 2001525. https://doi.org/10.1002/adem.202001525.
[38] G.D. Quinn, Weibull effective volumes and surfaces for cylindrical rods loaded in flexure, J. Am. Ceram. Soc. 86 [3] (2003) 475-479.
[39] M. Jonke, T. Klünsner, P. Supancic, W. Harrer, J. Glätzle, R. Barbist, R. Ebner, Strength of WC-Co hard metals as a function of the effectively tested volume, Int. J. Refract. Met. Hard Mater. 64 (2017) 219–224. http://dx.doi.org/10.1016/j.ijrmhm.2016.11.003.
[40] B. Lawn, Fracture of brittle solids, 2nd edition, Cambridge University Press, Melbourne (1993) 86-105.
[41] S.S. Scherrer, U. Lohbauer, A. Della Bona, A. Vichi, M.J. Tholey, J.R. Kelly, R. van Noort, P.F. Cesar, ADM guidance - Ceramics: guidance to the use of fractography in failure analysis of brittle materials, Dental mater. 33 (2017) 599-620. http://dx.doi.org/10.1016/j.dental.2017.03.004.
[42] A.G. Evans, D.R. Mumm, J.W. Hutchinson, G.H. Meier, F.S. Pettit, Mechanisms controlling the durability of thermal barrier coatings, Progr. Mater. Sci. 46 (2001) 505-553. https://doi.org/10.1016/S0079-6425(00)00020-7.
[43] Paul S. Addison, Fractals and Chaos - an Illustrated Course, Institute of Physics Publishing, London, 1997.
[44] C.Q. Yuan, J. Li, X.P. Yan, Z. Peng, The use of the fractal description to characterize engineering surfaces and wear particles, Wear 255 (2003) 315–326. https://doi.org/10.1016/S0043-1648(03)00206-0.
[45] T. Klünsner, T. Lube, C. Gettinger, L. Walch, R. Pippan, Influence of WC-Co hard metal microstructure on defect density, initiation and propagation kinetics of fatigue cracks starting at intrinsic and artificial defects under a negative stress ratio, Acta Mater. 188 (2020) 30-39. https://doi.org/10.1016/j.actamat.2020.01.057.
[46] T. Klünsner, M. Jonke, P. Supancic, C. Gettinger, M. Krobath, T. Lube, S. Marsoner, J. Glätzle, Fatigue behaviour of WC-Co hard metal under stress ratio and effectively loaded volume relevant to metalworking tool failure, Int. J. Refract. Met. Hard Mater. 80 (2019) 97–103. https://doi.org/10.1016/j.ijrmhm.2019.01.003.
[47] J. Kampichler, Z.L. Zhang, T. Klünsner, B. Sartory, J. Wosik, F. Nahif, Redeposition layer formation caused by shading effect during sputter cleaning and associated damage on rake face of TiN coated high-speed steel drills, Surf. Coat. Technol. 438 (2022) 128412. https://doi.org/10.1016/j.surfcoat.2022.128412.
[48] D.-d. Ma, Y.-p. Xue, J. Gao, Y. Ma, S.-w. Yu, Y.-s. Wang, C. Xue, H.-j. Hei, B. Tang, Effect of Ta diffusion layer on the adhesion properties of diamond coating on WC-Co

substrate, Appl. Surf. Sci. 527 (2020) 146727. https://doi.org/10.1016/j.apsusc.2020.146727.
[49] A.W. Nemetz, W. Daves, T. Klünsner, C. Praetzas, W. Liu, T. Teppernegg, C. Czettl, F. Haas, C. Bölling, J. Schäfer, Experimentally validated calculation of the cutting edge temperature during dry milling of Ti6Al4V, J. Mater. Process. Technol. 278 (2020) 116544, https://doi.org/10.1016/j.jmatprotec.2019.116544.